# Distorted Stability Space and Instability Triggering Mechanism of EV Aggregation Delays in the Secondary Frequency Regulation of Electrical Grid-Electric Vehicle System

Chaoyu Dong, Qian Xiao*, *Member*, *IEEE*, Mingshen Wang, *Student Member*, *IEEE*, Thomas Morstyn*, *Member*, *IEEE*, Malcom McCulloch, *Senior Member*, *IEEE*, Hongjie Jia *Senior Member*, *IEEE*

***Abstract*—Aggregated electric vehicles (EVs) are emerging as promising resources for the frequency regulation of the electrical grid, but the aggregation dynamics caused by various aggregation delays make unknown threats against the frequency stability. To address this stability uncertainty, a general aggregation-delay model is established for the electrical grid-electric vehicle system, which integrates heterogeneous-delay effect and reveals the sequential impact process of aggregation delays during the frequency regulation. To precisely visualize the aggregation delay influence, the maximum aggregation delay interval is discretized by the Chebyshev nodes, which formulates a delay distorted matrix reducing the infinite operator dimension. With this matrix, the damping ratio and the sensitivity indexes are then extracted constructing a complete workflow to characterize the asymptotic stability for EV aggregation delays. By the proposed approach, the distorted stability space and uniform target eigenvalue are accurately revealed in a typical electrical grid-electric vehicle system. It is also demonstrated that the aggregation delays infect the frequency stability through three unstable modes in a low-frequency oscillation form.**

***Index Terms*— Distorted stability space, aggregation delays, electric vehicles, delay distorted matrix, instability mode, sensitivity, uniform target eigenvalue.**

## I. Introduction

The penetration of electric vehicles (EVs) has been treated as a feasible way to provide the auxiliary frequency service without examining the aggregation delay concerns. The frequency of electrical grid plays an important role in the normal operation and maintenance of the whole electricity industry. As one of the main features of the alternating current, a unified frequency value is usually regulated at a national scale. The grid frequency in Great Britain and China is 50Hz, while America and Canada use 60Hz as the frequency standard. According to the National Electricity Transmission System Security and Quality of Supply Standard, the steady state of the grid frequency in the UK should fall in the limits between 49.5Hz and 50.5Hz [1]. The generating station acts once the frequency declines lower than 59.75Hz or rises higher than 60.25Hz directed by the PJM system operator in the US [2]. In China, the grid supplied by more than 3GW capacity generators should maintain the frequency deviation within 0.2Hz [3]. The time-varying changes in supplies and demands for electricity could have notable impacts on the grid frequency. On the basis of the data from GridWatch website [4] shown in Fig. 1, the UK grid frequency fluctuates frequently during 01-07 July 2019. The difference between the peak and valley had reached 0.15Hz within one week. If frequency accidents occur, load curtailments, frequency drops, or even blackouts might be triggered. Due to the decline of frequency to 48.88Hz, the blackout on 9-August-2019 disrupted around one million people in England and Wales [5]. Thousands of rail passengers were left stranded because of the electric train halt. As the operation and progress of whole society crucially depend on the electricity supply, it is important to guarantee the frequency stability of electrical grid.

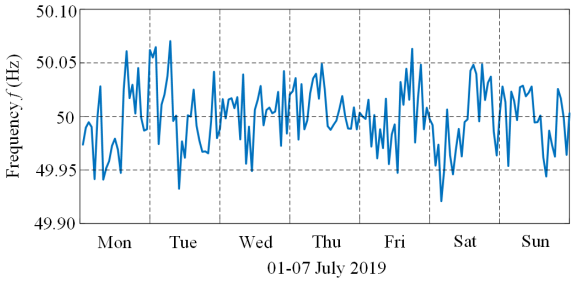


Fig. 1. Frequency fluctuation during 01-07 July 2019.

The development of battery technology boosts the boom of electric vehicles (EVs), which has attracted numerous attention in recent years. The battery technology has evolved from a strongly acidic or alkaline aqueous electrolyte with protons as the working ion to an organic liquid-carbonate electrolyte with $Li^+$ as the working ion in a Li-ion battery [6]. The $LiFePO_4$ cathode and the $Li_4Ti_5O_{12}$ anode have shown safe and rapid charge and discharge over many cycles [7]. In 2018, Telsa delivered a total of 245,240 vehicles: 145,846 Model 3 and

This work was supported in part by the Joint Project of National Natural Science Foundation of China and State Grid Corporation of China under Grant U1766210, in part by the National Natural Science Foundation of China under Grant 51625702. Paper no. TSG-01736-2019. (*Corresponding authors: Qian Xiao; Thomas Morstyn.*)

C. Dong, Q. Xiao, M. Wang, and H. Jia are with the Key Laboratory of Smart Grid of Ministry of Education, Tianjin University, Tianjin 300072, China, and also with the Key Laboratory of Smart Energy & Information Technology of Tianjin Municipality, Tianjin 300072, China (e-mail: cydong@tju.edu.cn, xiaoqian@tju.edu.cn, wangmingshen@tju.edu.cn, hjjia@tju.edu.cn).

T. Morstyn and M. McCulloch are with the Department of Engineering Science, University of Oxford, Oxford OX1 2JD, U.K (thomas.morstyn@eng.ox.ac.uk, malcolm.mcculloch@eng.ox.ac.uk).

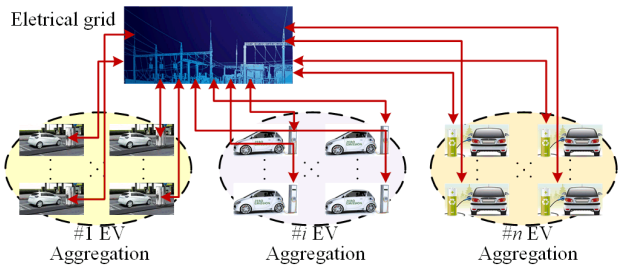


Fig. 2. EV aggregation in the electrical grid.

99,394 Model S and X [8], powered by lithium-ion cells from Panasonic [9]. In the national long-term development plan (2006–2020) of China, electric vehicles have been set as one of the prior themes [10]. The road range of EV600 vehicle from BYD has reached 520km [11]. With the increasing energy density and the sale volumes, EVs have the potential to participate in the secondary frequency regulation of the electricity grid shown by Fig. 2. Different from the inherent response of resources and load in the primary control facing short-term frequency changes in seconds, the secondary frequency regulation is a relatively long-term control, which aims to restore the grid to its scheduled frequency within the recovery period of 1-10mins [12]. Through the mixed integer linear programming, a power management scheme was developed for EVs to participate in the secondary frequency control [13]. On account of the uncertainties from energy and frequency regulation prices, the day-ahead dispatch and bidding size were investigated for EVs [14]. By the sliding-mode controller and the adaptive dynamic programming, the aggregated EVs and electricity grid were integrated for the long-term frequency deviation compensation [15]. Large-scale EV resources are aimed to be dispatched by those strategies to meet a minimum regulation capacity, which raises aggregation delay concerns.

During the aggregation process, the latency of EV power output is made up of several processes between the detection of a frequency fluctuation and the contribution of lumped EVs. According to the real-time frequency difference, the automatic generation control (AGC) system allocates the power ratios between aggregated EVs and electrical plant [16]. Receiving the dispatch signals, each EV aggregator then analyses the respective power command and available resources [17]. After the determination of EV number and locations, aggregation orders are distributed through the communication network guiding EV participation [18]. As the response chain consists of the deviation detection, AGC forming, aggregator dispatch, aggregation delays would be accumulated in the communication channels, which affects system performance.

To explore the delay impact on frequency regulation, some researchers have investigated different aspects. In [19], stability criteria are developed based on the Lyapunov theory and linear matrix inequality method to obtain a less conservative delay upper-bound. Lumping processing time and the measurement time as a single delay, simulations in [20] showed the time delay could lead to the failure of a frequency controller. Increasing the delay value in simulations, it reported that two identical delays during the EV dispatch might destabilize the frequency deviation [21]. As different EV aggregators could vary in terms of vehicle numbers, charging/discharging devices, power rates, and communication infrastructures, the frequency regulation process between the frequency deviation detection and the EV power generation would suffer from heterogeneous delays, especially for the aggregation of large EV numbers. Those heterogeneous delays would not only affect the power system operation due to the delayed frequency regulation power from EVs but also interact with each other to distort the stable operational space of the power system. Different from the conservative results obtained through the Lyapunov theory and linear matrix inequality method, eigenvalue-based methods determine the time-delay margin by computing purely imaginary roots of characteristic equations, which can deliver more exact results. The comparisons of Chebyshev polynomial, Pade approximation, the solution operator, and the linear multistep discretization in [22] concluded that Chebyshev approach was the most accurate and robust among those four methods. According to [23], the error of Chebyshev approximation is less than one-fourth of that caused by Pade approximation. Notwithstanding the merit of the Chebyshev polynomial, whether it is suitable for the stability analysis of EV aggregation, how to implement this technique, and the stability space feature have not been investigated so far.

To resolve the aggregation delay uncertainties and to investigate the feasibility of Chebyshev polynomial, this paper derives and investigates an aggregation-delay model for the electrical grid-electric vehicle system as well as its internal structure. The heterogeneous delays during the EV dispatch are characterized in terms of an infinite-dimensional operator. This is then replaced by Chebyshev polynomials of the first and the second kind so that a delay distorted matrix is formulated. On the basis of the delay distorted matrix, the damping ratio, oscillation frequency, and the parameter sensitivities are extracted, which generates a complete workflow for investigating the aggregation delay stability.

The contributions of this paper are summarized as follows.

1) Dissecting the EV aggregation delays into three sequential paths, i.e., control, combination, and coupling, the sequential impact process of heterogeneous delays is visualized and established to investigate the relationship between EV aggregation delays and grid frequency. In essence, it is found that heterogeneous aggregation delays misdirect the EV regulation process with asynchronous grid frequency signals, which disrupts the real-time EV aggregations.

**2) Accurate stability space determination.** The stability space determined by the proposed method is more accurate than existing methods. To accurately quantify the aggregation delay impact, the developed method directly formulates a delay distorted matrix integrating the electrical grid-electric vehicle system model and aggregation delays. Through the delay distorted matrix including the grid, EV statuses, and the aggregation delays, the accurate stability space can be presented revealing the stability space feature.

**3) Efficient stability assessment.** The implementation of the proposed method is more efficient compared with existing algorithms. As the stability assessment of heterogeneous delays is concentrated based on Chebyshev polynomials, the analysis result can be rapidly generated. The maximum delay-tolerant interval is mapped to a normalized interval, which reduces the

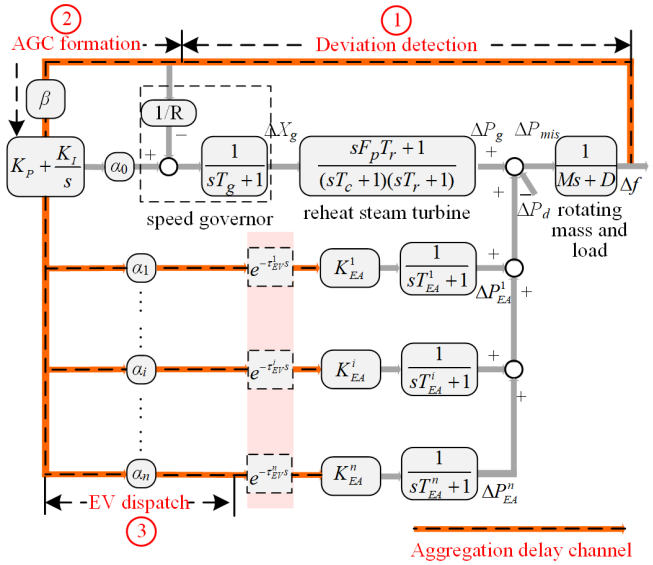


Fig. 3. System configuration with heterogeneous time delays.

infinite-dimensional operator induced by the delays. However, the existing stability criteria depend on the linear matrix inequality calculation, which require longer computation time to search matrices satisfying the conditional inequalities.

**4) Concise workflow design.** A new complete and computationally tractable workflow is proposed for the EV aggregation. The extracted damping ratio, oscillation frequency, and sensitivity comparison construct a concise stability analysis flow. It is easy and convenient for any dispatcher to assess the potential risk and consequence caused by the EV aggregation. The communication infrastructure can also be conveniently adjusted avoiding the unstable space.

**5) Instability mechanism discovery.** On the basis of the proposed approach, it is found that aggregation delays will trigger the electrical grid-electric vehicle system instability with a form of low-frequency oscillation, which gradually deteriorates the asymptotic stability forming the distorted stability space. The dominant eigenvalues and movement traces are determined, which reveals unstable modes due to EV aggregation delays in a particular set of cases. From the three aspects of instability mechanism, triggering form, and stability space shape, this work provides a complete reference for the EV aggregation delay investigation.

## II. Aggregation-delay Model of Electrical Grid-Electric Vehicle System

The large-scale EV aggregation provides a virtual dispatchable resource for the frequency regulation of electrical grid. To reveal the impact mechanism of time delays, the system configuration and the time-delay issue are illustrated from the model structure aspect.

### *A. Heterogeneous Time Delays during EV Aggregations*

Lumping the power plant and EV aggregators [19], the grid frequency dynamic is presented in Fig. 3, in which the electrical grid consists of speed governor, reheat steam turbine, rotating mass and load [27]. Because of the real-time power mismatch between generator output $\Delta P_g(t)$ and demand $\Delta P_d(t)$, the frequency $f(t)$ is disturbed in the following form

$$\Delta\dot{f}(t) = -\frac{D}{M}\Delta f(t) + \frac{1}{M}[\Delta P_g(t) - \Delta P_d(t)] \quad (1)$$

where $M$ and $D$ are the lumped inertia and damping coefficients of the electrical grid.

According to the instant frequency deviation, the valve position $\Delta X_g(t)$ of the speed governor is continuously adjusted via the drop coefficient $R$

$$\Delta\dot{X}_g(t) = -\frac{1}{RT_g}\Delta f(t) - \frac{1}{T_g}\Delta X_g(t) \quad (2)$$

On account of the time constant $T_c$ from main inlet volumes and steam chest, the power $\Delta P_s(t)$ of high-pressure and high-temperature steam is obtained as

$$\Delta\dot{P}_s(t) = -\frac{1}{T_c}\Delta P_s(t) + \frac{1}{T_c}\Delta X_g(t) \quad (4)$$

Crossing the reheater, the turbine generates the power $\Delta P_g(t)$ to compensate the power fluctuation

$$\Delta\dot{P}_g(t) = \frac{F_p\Delta X_g(t)}{T_c} - \frac{\Delta P_g(t)}{T_r} + \frac{T_c - F_pT_r}{T_rT_c}\Delta P_s(t) \quad (3)$$

where $T_r$ is the reheater time constant, $F_p$ is the fraction of total turbine power generated by high-pressure part.

Detecting the difference between real-time frequency and the rating value, the area control error ACE($t$) signal of the power system is obtained with the bias factor $\beta$

$$ACE(t) = \beta\Delta f(t) \quad (5)$$

Receiving the error signal in (5), the dispatch center forms the automatic generation control (AGC) command via the proportional-integral (PI) process

$$AGC(t) = -K_P ACE(t) - K_I\int ACE(t)dt \quad (6)$$

where $K_P$ indicates the suppression of current ACE value, $K_I$ is tasked to cope with the accumulated frequency deviation.

According to the dispatch command in (6) and the allocation coefficients $\alpha_0$, $\alpha_1$,…, $\alpha_i$, …, $\alpha_n$, the control center regulates the electrical grid and EV aggregators with the following signals

$$u_i(t) = \alpha_i AGC(t),\ i=0,\ldots,n \quad (7)$$

With (6)-(7), it can be seen that the equivalent control gains for the $i^{th}$ EV aggregator is $K_P^i = \alpha_i K_P$ and $K_I^i = \alpha_i K_I$, which can be flexibly adjusted with different $\alpha_i$ for different electric vehicle aggregators.

Seen from Fig. 3, the aggregation of EVs experiences three time-consuming procedures: deviation detection ($\tau_{c1}$), AGC formation ($\tau_{c2}$), and EV dispatch ($\tau_{c3}$). $\tau_{c1}$, $\tau_{c2}$, and $\tau_{c3}$ are the delays associated with these processes. Because of the different communication channels and schedules adopted by different aggregators, the EV dispatch delay may vary for each aggregator leading to $\tau_{c3}^i$, $i$=1,…,$n$. Lumped with $\tau_{c1}$ and $\tau_{c2}$, the aggregation delay value for the $i^{th}$ EV is obtained as

$$\tau_{EV}^i = \tau_{c1} + \tau_{c2} + \tau_{c3}^i \quad (8)$$

Due to these embedded delays in (8), each EV regulation signal in (7) has to be rewritten as

$$u_i(t-\tau_{EV}^i) = -\alpha_i K_P ACE(t-\tau_{EV}^i) - \alpha_i K_I\int_0^t ACE(t-\tau_{EV}^i)dt \quad (9)$$

Substituting (5) into (9), the delayed command is related to the past frequency deviation in essence

$$u_i(t-\tau_{EV}^i) = -\alpha_i\beta[K_P\Delta f(t-\tau_{EV}^i) + K_I\int_0^t \Delta f(t-\tau_{EV}^i)dt] \quad (10)$$

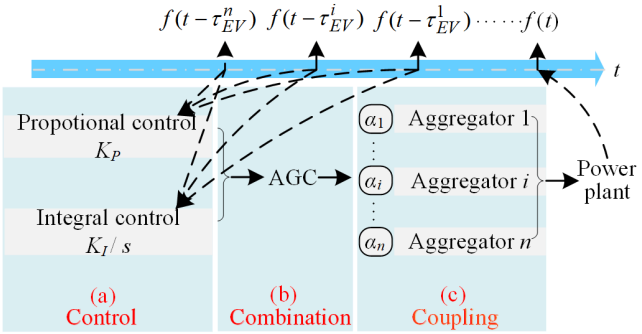


Fig. 4. Sequential impact process of heterogeneous aggregation delays.

From (10), it can be seen that various time delays penetrate the system dynamics through three sequential paths in Fig. 4:

1) Control: the past frequency state is detected and regulated with proportional coefficient $K_P$ or integral coefficient $K_I$, respectively. Different from the instant delay impact in the proportional controller $K_P\Delta f(t-\tau_{EV}^i)$, the delay impact continuously accumulates in the second item of (10), i.e., $K_I\int\Delta f(t-\tau_{EV}^i)dt$. The response speed and the error elimination process are both affected.

2) Combination: apart from the individual impact from $K_P\Delta f(t-\tau_i)$ or $K_I\int\Delta f(t-\tau_i)dt$, these two dynamics are combined simultaneously in (10), which distorts the dispatch command together.

3) Coupling: since various EV aggregators participate in the frequency regulation, multiple aggregation delays couple indirectly through respective regulation routes. Since the aggregation processes of different EV aggregators could vary with vehicle numbers, charging/discharging states, power ranges, and communication infrastructures, their aggregation delays cannot be assumed with an identical delay value $\tau$ for all the aggregators. Therefore, independent variables $\tau_{EV}^1,\ldots,\tau_{EV}^n$ are employed to reflect these heterogeneous delays for EV aggregators.

The $K_P$ and $K_I$ controllers reflect the AGC components for instant deviation and accumulative deviation regulations, respectively. It should be mentioned that the control and combination paths actually affects the stability of the system simultaneously. The dissection of these two paths is to indicate $K_P$ and $K_I$ might interact differently with aggregation delays.

After aggregators cluster available EVs to participate in the frequency service, the first-order transfer function in [21] is employed to indicate the EV battery dynamics

$$G_{EV}^i(s)=\frac{K_{EV}^i}{1+sT_{EV}^i} \tag{11}$$

where $K_{EV}^i$ is the battery coefficient of the $i^{th}$ EV aggregator, $T_{EV}^i$ is the corresponding battery time constant.

Because of the time-delay influence, the power contribution from the $k^{th}$ aggregation group is then distorted as

$$\Delta\dot{P}_{EV}^i(t)=-\frac{1}{T_{EV}^i}\Delta P_{EV}^i(t)+\frac{K_{EV}^i}{T_{EV}^i}u_i(t-\tau_{EV}^i) \tag{12}$$

With (12), heterogeneous time delays $\tau_{EV}^1,\ldots,\tau_{EV}^n$ during the aggregation process insert into the electrical grid determining the real-time power mismatch $\Delta P_{mis}$

$$\Delta P_{mis}(t)=\Delta P_g(t)+\sum_{i=1}^n\Delta P_{EV}^i(t)-\Delta P_d(t) \tag{13}$$

The whole heterogeneous time-delay loop is closed by (13) from the aggregation procedure to the power.

### *B. Aggregation-delay Model for EV Regulation System*

To further investigate the impact of aggregation delay on the whole system, the non-delay part, i.e., the electrical grid, is first modeled. Denoting $[\Delta f(t),\Delta P_g(t),\Delta P_s(t),\Delta X_g(t),\int\Delta ACE(t)dt]^T$ as the grid state vector $\boldsymbol{x}_{EG}(t)$, the non-delay model of electrical grid is derived combining (1)-(7)

$$\dot{\boldsymbol{x}}_{EG}(t)=\boldsymbol{A}_{EG}\boldsymbol{x}_{EG}(t)+\boldsymbol{B}_{EG}\Delta\boldsymbol{P}_{EV}(t)+\boldsymbol{F}_{EG}\Delta P_d(t) \tag{14}$$

where

$$\boldsymbol{A}_{EG}=\begin{bmatrix}-\frac{D}{M}&\frac{1}{M}&0&0&0\\0&-\frac{1}{T_r}&\frac{T_c-F_PT_r}{T_rT_c}&\frac{F_P}{T_c}&0\\0&0&-\frac{1}{T_c}&\frac{1}{T_c}&0\\-\frac{1+\alpha_0\beta RK_P}{RT_g}&0&0&-\frac{1}{T_g}&-\frac{\alpha_0K_I}{T_g}\\\beta&0&0&0&0\end{bmatrix},$$

$$\boldsymbol{B}_{EG}=\begin{bmatrix}\frac{1}{M}&\cdots&\frac{1}{M}&\cdots&\frac{1}{M}\\0&\cdots&0&\cdots&0\\\vdots&\ddots&\vdots&\ddots&\vdots\\\vdots&\ddots&\vdots&\ddots&\vdots\\0&\cdots&0&\cdots&0\end{bmatrix},\boldsymbol{P}_{EV}=\begin{bmatrix}P_{EV}^1\\\vdots\\P_{EV}^i\\\vdots\\P_{EV}^n\end{bmatrix},\boldsymbol{F}_{EG}=\begin{bmatrix}-\frac{1}{M}\\0\\\vdots\\\vdots\\0\end{bmatrix}.$$

Without the injection of aggregation delays, the deviations of system states can be seen from (14), which is represented by a linear differential equation. However, heterogeneous time delays during the EV aggregations penetrate through the $\boldsymbol{P}_{EV}$. Setting the EV variables $\boldsymbol{x}_{EV}(t)=[\Delta P_{EV}^1(t),\ldots,\Delta P_{EV}^n(t)]^T$, the state of EV aggregation system is established via (8)-(12)

$$\dot{\boldsymbol{x}}_{EV}(t)=\boldsymbol{A}_{EV}\boldsymbol{x}_{EV}(t)+\sum_{i=1}^n\boldsymbol{B}_{EV}^iAGC(t-\tau_{EV}^i) \tag{15}$$

where

$$\boldsymbol{A}_{EV}=\begin{bmatrix}-\frac{1}{T_{EV}^1}&\cdots&0&\cdots&0\\\vdots&\ddots&\vdots&\ddots&\vdots\\0&\cdots&-\frac{1}{T_{EV}^i}&\cdots&0\\\vdots&\ddots&\vdots&\ddots&\vdots\\0&\cdots&0&\cdots&-\frac{1}{T_{EV}^n}\end{bmatrix},\boldsymbol{B}_{EV}^i=\begin{bmatrix}0\\\vdots\\\frac{\alpha_iK_{EV}^i}{T_{EV}^i}\\\vdots\\0\end{bmatrix}.$$

As shown in (15), the delayed system states are merged with $\boldsymbol{B}_{EV}^1,\ldots,\boldsymbol{B}_{EV}^i,\ldots,\boldsymbol{B}_{EV}^n$. The impact transmission channel of control, combination, and coupling in Fig. 4 are indicated with

$\sum_{i=1}^{n} \boldsymbol{B}_{EV}^{i} \boldsymbol{x}_{EV}(t-\tau_i)$. Substituting (15) into (14), the aggregation delay model of hybrid system is established

$$\dot{\boldsymbol{x}}(t) = \boldsymbol{A}\boldsymbol{x}(t) + \sum_{i=1}^{n} \boldsymbol{A}_i \boldsymbol{x}(t-\tau_{EV}^{i}) + \boldsymbol{F}\Delta P_d(t) \tag{16}$$

where $\boldsymbol{x}(t) = [\boldsymbol{x}_{EG}, \boldsymbol{x}_{EV}]^T$,

$$\boldsymbol{A} = \begin{bmatrix} \frac{-D}{M} & \frac{1}{M} & 0 & 0 & 0 & \frac{1}{M} & \cdots & \frac{1}{M} \\ 0 & \frac{-1}{T_r} & \frac{T_c - F_p T_r}{T_r T_c} & \frac{F_p}{T_c} & 0 & 0 & \cdots & 0 \\ 0 & 0 & \frac{-1}{T_c} & \frac{1}{T_c} & 0 & 0 & \cdots & 0 \\ -\frac{1+\alpha_0 \beta R K_P}{R T_g} & 0 & 0 & \frac{-1}{T_g} & -\frac{\alpha_0 K_I}{T_g} & 0 & \cdots & 0 \\ \beta & 0 & 0 & 0 & 0 & 0 & \cdots & 0 \\ 0 & 0 & 0 & 0 & 0 & \frac{-1}{T_{EV}^{1}} & \cdots & 0 \\ \vdots & \vdots & \vdots & \vdots & \vdots & \vdots & \ddots & \vdots \\ 0 & 0 & 0 & 0 & 0 & 0 & \cdots & \frac{-1}{T_{EV}^{n}} \end{bmatrix},$$

$$\boldsymbol{A}_i = \begin{bmatrix} 0 & 0 & 0 & 0 & 0 & 0 & \cdots & 0 & \cdots & 0 \\ 0 & 0 & 0 & 0 & 0 & 0 & \ddots & \vdots & \ddots & 0 \\ 0 & 0 & 0 & 0 & 0 & 0 & \cdots & 0 & \cdots & 0 \\ 0 & 0 & 0 & 0 & 0 & 0 & \ddots & \vdots & \ddots & 0 \\ 0 & 0 & 0 & 0 & 0 & 0 & \cdots & 0 & \cdots & 0 \\ 0 & 0 & 0 & 0 & 0 & 0 & \cdots & 0 & \cdots & 0 \\ \vdots & \ddots & \ddots & \ddots & \vdots & \vdots & \ddots & \vdots & \ddots & \vdots \\ -\frac{\alpha_i \beta K_{EV}^{i} K_P}{T_{EV}^{i}} & 0 & 0 & 0 & -\frac{\alpha_i K_{EV}^{i} K_I}{T_{EV}^{i}} & 0 & \cdots & 0 & \cdots & 0 \\ \vdots & \ddots & \ddots & \ddots & \vdots & \vdots & \ddots & \vdots & \ddots & \vdots \\ 0 & 0 & 0 & 0 & 0 & 0 & \cdots & 0 & \cdots & 0 \end{bmatrix}, \quad \boldsymbol{F} = \begin{bmatrix} \frac{-1}{M} \\ 0 \\ 0 \\ 0 \\ 0 \\ 0 \\ \vdots \\ 0 \\ \vdots \\ 0 \end{bmatrix}.$$

Different from (14) and (15), several very sparse matrices $\boldsymbol{A}_i$ ($i$ = 1,2,…,$n$) are formed in (16). With the increasing number of EV aggregators, there would be more and more time delays to interact in the frequency regulation system. As pointed by the three sequential impact processes of heterogeneous delays, aggregation delays essentially mislead the control center to dispatches based on asynchronous frequency deviations, which raises two stability concerns:

1) Instability approach: If time delays are ignored, $\boldsymbol{A}$ and $\boldsymbol{A}_1$,…, $\boldsymbol{A}_i$,…, $\boldsymbol{A}_n$ could be directly added as a whole matrix. Nevertheless, due to the disorder caused by $\tau_{EV}^{1}$,…, $\tau_{EV}^{n}$, these coefficients are separated from ($\boldsymbol{A}$+$\boldsymbol{A}_1$+…+$\boldsymbol{A}_i$+…+$\boldsymbol{A}_n$). As the original non-delay model has been transformed into a heterogeneous-delay model, it is necessary to figure out the change caused by the aggregation delays triggering the frequency instability.

2) Stability space: According to the instability mechanism, the accurate assessment of stability space is critical for the normal operation of power system with EVs integration.

The approach shown in Fig. 5 has three components: the sequential process of delay impact, instability triggering mechanism, and precise stability space. The descriptions of instability triggering mechanism and precise stability space are detailed in Section 3 with the proposed workflow, which constructs a clear and complete stability assessment for the large-scale aggregation of EVs in the frequency regulation.

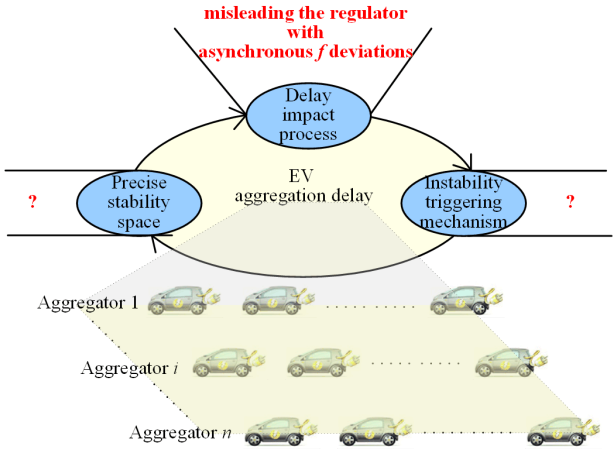


Fig. 5. Stability uncertainties caused by the aggregation delays.

## III. Delay-dependent Aggregation Delay Stability Analysis

As the coupling of aggregation delays and the time in the EV regulation model (16), the direct analysis of asymptotic stability is challenging. To remove this burden for the investigation of triggering mechanism and stability space, the non-delay and delay components in the system model are firstly integrated to an infinite-dimensional operator, which uniformly presents the delay and the system features. To further reduce the analysis dimension, the Chebyshev polynomials are then employed transforming this operator to a finite-dimensional delay distorted matrix. By the formulation of this matrix, the original coupling of aggregation delays and the time is represented discretely, which contributes to the concise workflow establishment of stability analysis.

### A. Delay Distorted Matrix

If a transition time step $T \in [0, \tau_{EV}^{\max}]$ is set, $\tau_{EV}^{\max} = \max(\tau_{EV}^{i}, i = 1,\ldots,n)$, the system state transition could be classified into two parts according to (16):

If $t \in [-\tau_{EV}^{\max}, -T]$, $t+T \in [-\tau_{EV}^{\max}+T, 0]$. As (16) is only activated after $t$>0, the electrical grid and EV states would maintain to be the initial ones $\boldsymbol{X}(0)$. The aggregation delays

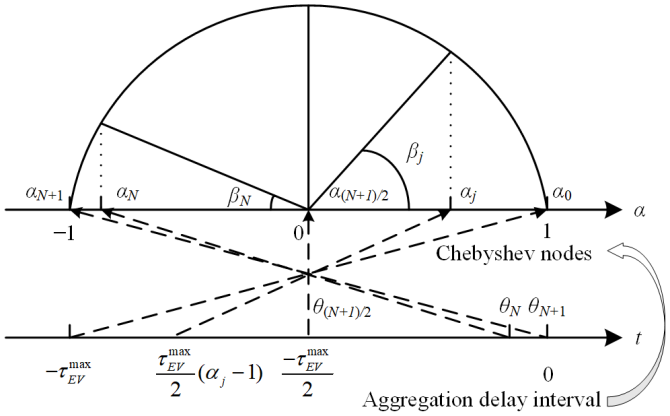


Fig. 6. Chebyshev node discretization on aggregation delay interval.

would not affect the asymptotic stability of the regulation system.

If $t \in [-T, +\infty]$, $t+T > 0$. Since (16) is activated, the whole system changes are represented as an integral equation

$$\boldsymbol{x}(t) = \boldsymbol{X}(0) + \int_0^t \boldsymbol{A}\boldsymbol{x}(h) + \sum_{i=1}^{n} \boldsymbol{A}_i \boldsymbol{x}(h-\tau_{EV}^i) + \boldsymbol{F}\Delta P_d(h)dh \quad (17)$$

Equation (17) is the time-domain solution of the aggregation-delay model. Given the initial system state $\boldsymbol{X}(0)$ and the external disturbance $P(t)$, the asymptotic stability of this system is determined by the coefficients $\boldsymbol{A}$, $\boldsymbol{A}_i$, $i = 1,\ldots,n$ and the aggregation delays $\tau_{EV}^1,...,\tau_{EV}^n$. To further transform the asymptotic stability analysis of this time-domain solution to the investigation of eigenvalue locations, introducing an infinite-dimensional operator $\boldsymbol{\mathcal{A}}$ [24], an abstract ordinary differential equation (18) can be established

$$\dot{\boldsymbol{x}}(t+\xi) = \boldsymbol{\mathcal{A}}\boldsymbol{x}(t+\xi) \quad (18)$$

where $\xi \in [-\tau_{EV}^{\max}, 0]$. According to (17)-(18), it can be found that the aggregation delay impact is initialized at the last delay interval $[-T, +\infty]$, which introduces an infinite-dimensional operator. Due to the items $\boldsymbol{x}_{EV}(t-\tau_{EV}^i)$, $i=1,\ldots,n$, the finite-dimensional operator $(\boldsymbol{A}+\boldsymbol{A}_1+\ldots+\boldsymbol{A}_n)$ is replaced by an infinite-dimensional operator $\boldsymbol{\mathcal{A}}$, which distorts the original finite-dimensional model.

To further explore the delay impact, the maximum aggregation delay interval $[-\tau_{EV}^{\max}, 0]$ is interpolated with the points of $\theta_0,\ldots, \theta_j,\ldots, \theta_{N+1}$ in Fig. 6 to reduce the model dimension. A point-to-point mapping is established between the delay interval and the Chebyshev nodes within [-1, 1]

$$\theta_j = \frac{\tau_{EV}^{\max}}{2}(\alpha_j - 1) \quad (19)$$

where $\alpha_j = -\cos\frac{\pi j}{N+1}$, $j = 0, \ldots, N$ are shift coefficients. The interpolation points are reflected by $\alpha_j$ within [-1, 1].

Denoting $\beta_j = \arccos(\alpha_j)$, the $N^{th}$-order Chebyshev poly nomials of the first and the second kind are then obtained [25]

$$T_N(\alpha_j) = \cos N\beta_j \quad (20)$$

$$U_N(\alpha_j) = \frac{\sin(N+1)\beta_j}{\sin\beta_j} \quad (21)$$

According to the normalized points $\alpha_0,\ldots, \alpha_j,\ldots, \alpha_{N+1}$ corresponding to $N$+1 Chebyshev nodes, the grid and EV states $\boldsymbol{x}(t)$ in the range of $[t-\tau_{EV}^{\max}, 0]$ is discretized into $N$+1 state variables $\boldsymbol{x}(t+\theta_0),...,\boldsymbol{x}(t+\theta_j),...,\boldsymbol{x}(t+\theta_N)$. Transcendental items $\boldsymbol{x}(t-\tau_{EV}^i)$, $i=1,\ldots,n$, resulted from the aggregation delays are simulated with $N^{th}$-order Chebyshev polynomials

$$\boldsymbol{x}(t-\tau_{EV}^i) = \sum_{j=0}^{N} c_j T_j[\frac{2(t-\tau_{EV}^i)}{\tau_{EV}^{\max}} + 1]\boldsymbol{x}(t+\theta_j) \quad (22)$$

Considering the dynamic model (16) of $\boldsymbol{x}(t)$ and the interpolation states $\boldsymbol{x}(t+\theta_0),...,\boldsymbol{x}(t+\theta_j),...,\boldsymbol{x}(t+\theta_N)$, the connection between $\boldsymbol{x}(t)$ and the previous states can be established as

$$\dot{\boldsymbol{x}}(t) = \boldsymbol{A}\boldsymbol{x}(t) + \sum_{i=1}^{n} \boldsymbol{A}_i \sum_{j=0}^{N} c_j T_j[\frac{2(t-\tau_{EV}^i)}{\tau_{EV}^{\max}} + 1]\boldsymbol{x}(t+\theta_j) \quad (23)$$

As the asymptotic stability is consistent along $[0, \infty)$, the $t$ in (23) can be shifted to 0 for the analysis. In the meantime, the interpolation states in (23) are differentiated on account of the relationship between the first and the second kind Chebyshev polynomials, i.e., $\dot{T}_N(\alpha_j) = NU_{N-1}(\alpha_j)$, which derives the dynamic equations for $\boldsymbol{x}(\theta_j)$, $j$=1,…, $N$

$$\begin{bmatrix} \dot{\boldsymbol{x}}(\theta_1) \\ \vdots \\ \dot{\boldsymbol{x}}(\theta_N) \end{bmatrix} = \begin{bmatrix} U_0(\alpha_1)\boldsymbol{I}_n & \cdots & NU_0(\alpha_1)\boldsymbol{I}_n \\ \vdots & \ddots & \vdots \\ U_0(\alpha_N)\boldsymbol{I}_n & \cdots & NU_0(\alpha_1)\boldsymbol{I}_n \end{bmatrix} \begin{bmatrix} \boldsymbol{x}(\theta_1) \\ \vdots \\ \boldsymbol{x}(\theta_N) \end{bmatrix} \quad (24)$$

Combining (23) and (24), the system model for the asymptotic stability is formulated introducing the new state variables $\boldsymbol{x}_N(0) = \left[\boldsymbol{x}^T(0) \quad \boldsymbol{x}^T(\theta_1) \quad \cdots \quad \boldsymbol{x}^T(\theta_N)\right]^T$ removing the transcendental items caused by the aggregation delays

$$\begin{bmatrix} \boldsymbol{A}_0 c_0 T_0(1) + \sum_{i=1}^{n} \boldsymbol{A}_k c_0 T_0(-\frac{2\tau_{EV}^i}{\tau_{EV}^{\max}} + 1) & \boldsymbol{A}_0 c_1 T_1(1) + \sum_{i=1}^{n} \boldsymbol{A}_k c_1 T_1(-\frac{2\tau_{EV}^i}{\tau_{EV}^{\max}} + 1) \\ \boldsymbol{O}_{n\times n} & \boldsymbol{U}_0(\alpha_1) \\ \vdots & \vdots \\ \boldsymbol{O}_{n\times n} & \boldsymbol{U}_0(\alpha_N) \end{bmatrix}$$

$$\begin{matrix} \cdots & \boldsymbol{A}_0 c_N T_N(1) + \sum_{i=1}^{n} \boldsymbol{A}_k c_N T_N(-\frac{2\tau_{EV}^i}{\tau_{EV}^{\max}} + 1) \\ \cdots & \boldsymbol{N}\boldsymbol{U}_0(\alpha_1) \\ \ddots & \vdots \\ \cdots & \boldsymbol{N}\boldsymbol{U}_0(\alpha_N) \end{matrix} \begin{bmatrix} \boldsymbol{x}(0) \\ \boldsymbol{x}(\theta_1) \\ \vdots \\ \boldsymbol{x}(\theta_N) \end{bmatrix} = \dot{\boldsymbol{x}}_N(0) \quad (25)$$

With (25), the infinite-dimensional characteristic equation for (18) is then reduced to $(N+1)(n+5)$ dimension [26]

$$\det\left\{ \lambda \begin{bmatrix} 1 & T_1(1) & \cdots & T_{N-1}(1) & T_N(1) \\ 1 & T_1(\alpha_1) & \cdots & T_{N-1}(\alpha_1) & T_N(\alpha_1) \\ \vdots & \vdots & \vdots & \vdots & \vdots \\ \vdots & \vdots & \vdots & \vdots & \vdots \\ 1 & T_1(\alpha_N) & \cdots & T_{N-1}(\alpha_N) & T_N(\alpha_N) \end{bmatrix} \otimes \boldsymbol{I}_{n+5} - \right.$$

$$\left. \begin{bmatrix} \boldsymbol{R}_0 & \boldsymbol{R}_1 & \boldsymbol{R}_2 & \cdots & \boldsymbol{R}_N \\ 0 & \frac{2}{\tau_{EV}^{\max}} U_0(\alpha_1) I_{n+5} & \frac{4}{\tau_{EV}^{\max}} U_1(\alpha_1) I_{n+5} & \cdots & \frac{2N}{\tau_{EV}^{\max}} U_{N-1}(\alpha_1) I_{n+5} \\ \vdots & \vdots & \vdots & \vdots & \vdots \\ \vdots & \vdots & \vdots & \vdots & \vdots \\ 0 & \frac{2}{\tau_{EV}^{\max}} U_0(\alpha_N) I_{n+5} & \frac{4}{\tau_{EV}^{\max}} U_1(\alpha_N) I_{n+5} & \cdots & \frac{2N}{\tau_{EV}^{\max}} U_{N-1}(\alpha_N) I_{n+5} \end{bmatrix} \right\} = 0 \quad (26)$$

where $\boldsymbol{R}_N = \boldsymbol{A} + \sum_{i=1}^{n} \boldsymbol{A}_i \boldsymbol{T}_N(-\frac{2\tau_{EV}^i}{\tau_{EV}^{\max}} + 1)$, $\otimes$ is the Kronecker product.

Considering the relationship between the first and second kind Chebyshev polynomials $T_1(\alpha_j)=0.5U_1(\alpha_j)$, $T_N(\alpha_j)=0.5U_N(\alpha_j)-0.5U_{N-2}(\alpha_j)$, $N>2$, the eigenvalue constraint in (26) can then be transformed to

$$\det(\lambda\prod_N - \sum_N) = 0 \quad (27)$$

where $\boldsymbol{\Pi}_N \in \mathbb{R}^{(N+1)n\times(N+1)n}$ is a companion-type matrix and $\boldsymbol{\Sigma}_N \in \mathbb{R}^{(N+1)n\times(N+1)n}$ is a block upper triangular matrix,

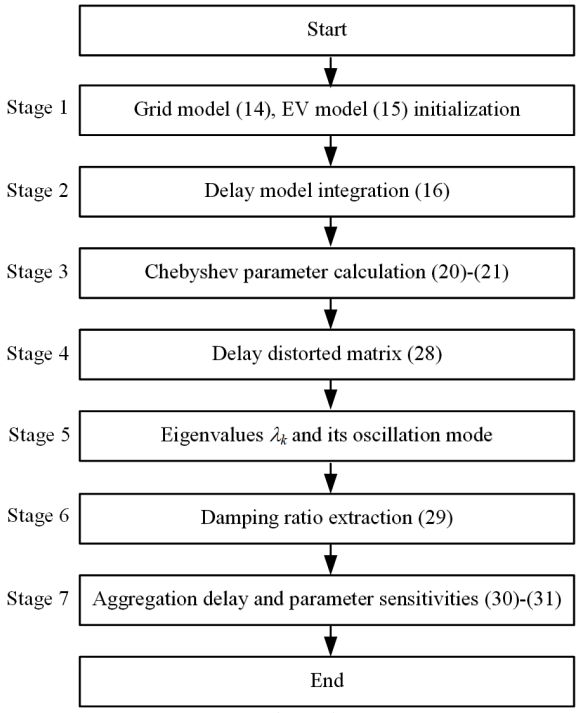


Fig. 7. Asymptotic stability analysis flow of EV aggregation delays.

$$\boldsymbol{\Pi}_N = \frac{\tau_{\max}}{4}\begin{bmatrix} \frac{4}{\tau_{\max}} & \frac{4}{\tau_{\max}} & \frac{4}{\tau_{\max}} & \frac{4}{\tau_{\max}} & \cdots & \frac{4}{\tau_{\max}} & \frac{4}{\tau_{\max}} \\ 2 & 0 & -1 & 0 & \cdots & 0 & 0 \\ 0 & \frac{1}{2} & 0 & -\frac{1}{2} & \ddots & 0 & 0 \\ 0 & 0 & \frac{1}{3} & 0 & \ddots & 0 & 0 \\ 0 & 0 & 0 & \frac{1}{4} & \ddots & -\frac{1}{N-2} & 0 \\ \vdots & \vdots & \vdots & \ddots & \ddots & 0 & \vdots \\ 0 & 0 & 0 & 0 & \cdots & \frac{1}{N} & 0 \end{bmatrix} \otimes \boldsymbol{I}_{n+5},$$

$$\boldsymbol{\Sigma}_N = \begin{bmatrix} \boldsymbol{R}_0 & \boldsymbol{R}_1 & \cdots & \boldsymbol{R}_j & \cdots & \boldsymbol{R}_N \\ \boldsymbol{O}_{n+5} & \boldsymbol{I}_{n+5} & \boldsymbol{O}_{n+5} & \cdots & \cdots & \boldsymbol{O}_{n+5} \\ \vdots & \ddots & \ddots & \ddots & \ddots & \vdots \\ \boldsymbol{O}_{n+5} & \ddots & \ddots & \boldsymbol{I}_{n+5} & \ddots & \boldsymbol{O}_{n+5} \\ \vdots & \ddots & \ddots & \ddots & \ddots & \vdots \\ \boldsymbol{O}_{n+5} & \boldsymbol{O}_{n+5} & \cdots & \boldsymbol{O}_{n+5} & \cdots & \boldsymbol{I}_{n+5} \end{bmatrix}.$$

The delay distorted matrix is formed to reflect the frequency variations and EV aggregation delays

$$\boldsymbol{A}_N = \boldsymbol{\Pi}_N^{-1}\boldsymbol{\Sigma}_N \tag{28}$$

It can be seen from (28) that at least $N(n+5)$ extra variables will be triggered by the EV aggregation delays, which adds on the original frequency fluctuations. Since the aggregation delays $\tau_{EV}^1$ ,…, $\tau_{EV}^n$ are involved in the $\boldsymbol{A}_N$, the developed stability analysis is delay-dependent.

### *B. Damping Ratio and Oscillation Frequency Extraction*

With the delay distorted matrix $\boldsymbol{A}_N$ of $(N+1)(n+5) \times (N+1)(n+5)$ dimension, the eigenvalues of this time-delay system can be calculated showing its asymptotic stability status.

As eigenvalues are usually expressed in the conjugate form of $\lambda_k = \sigma_k \pm j\omega_k$, it is feasible to determine the oscillation modes of the system. If the real part $\sigma_k$ is positive, the oscillation of the system will increase. The frequency fluctuation attenuates with a negative $\sigma_k$. The oscillation frequency is determined by the imaginary part of the eigenvalue $f_k = \omega_k/2\pi$, and the corresponding damping ratio is [27]

$$\xi_k = -\sigma_k / \sqrt{\sigma_k^2 + \omega_k^2} \tag{29}$$

When $\xi_k < 0$, the eigenvalue reflects an unstable oscillation mode; when $\xi_k = 0$, it causes the persistent oscillation of grid frequency; when $\xi_k > 0$, the eigenvalue does not lead to the frequency instability. The larger damping ratio indicates a more stable status. The eigenvalue with the maximum real part is the dominant one, which directly influences the frequency.

### *C. Aggregation Delays and Parameter Sensitivities*

Denoting $\lambda_k$ as one eigenvalue of the delay distorted matrix $\boldsymbol{A}_N$, its normalized sensitivity with respect to aggregation delay can be obtained as

$$\frac{\partial \lambda_k}{\partial \tau_{EV}^i} = \frac{\left[\lambda_k(\tau_{EV}^i + \Delta\tau_{EV}^i) - \lambda_k(\tau_{EV}^i)\right] / \left|\lambda_k(\tau_{EV}^i)\right|}{\Delta\tau_{EV}^i / \left|\tau_{EV}^i\right|} \tag{30}$$

where $\Delta\tau_{EV}^i$ is the delay increment for $i^{th}$ EV aggregator.

Similarly, the normalized sensitivity of $\lambda_k$ with respect to other parameter $p_l$ is derived in (31)

$$\frac{\partial \lambda_k}{\partial p_l} = \frac{\left[\lambda_k(p_l + \Delta p_l) - \lambda_k(p_l)\right] / \left|\lambda_k(p_l)\right|}{\Delta p_l / \left|p_l\right|} \tag{31}$$

On the basis of (30)-(31), the correlation of system parameters with delay stability can be quantitatively assessed through the sensitivities calculation. This helps to establish the complete stability analysis flow in Section III.D and discover the dominant reason for instability triggering the aggregation delay instability.

### *D. Asymptotic Stability Analysis Flow*

With the EV aggregation model (15), aggregation-delay model (16) in Section II and stability analysis approaches (20)-(31), the analysis flow for the asymptotic stability of electrical grid-electric vehicle system is shown in Fig. 7, which organizes the whole quantitative analysis procedures in seven stages.

## IV. Case Studies

TABLE I ELECTRICAL GRID-ELECTRIC VEHICLE SYSTEM PARAMETERS

| Parameters | Values |
|---|---|
| Inlet and steam chest constant $T_c$ | 0.3 |
| Reheater constant $T_r$ | 12 |
| High pressure fraction $F_p$ | 1/6 |
| Governor constant $T_g$ | 0.2 |
| Inertia constant $M$ | 8.8 |
| Damping coefficient $D$ | 1 |
| Droop coefficient $R$ | 1/11 |
| Bias factor $\beta$ | 21 |
| Grid contribution rate $\alpha_0$ | 0.8 |
| Aggregator 1 rate $\alpha_1$ | 0.1 |
| Aggregator 2 rate $\alpha_1$ | 0.1 |
| Charging/discharging coefficient $K_{EA}^1$, $K_{EA}^2$ | 1 |
| Battery time constant $T_{EA}^1$, $T_{EA}^2$ | 0.1 |

### A. *Electrical Grid-Electric Vehicle System*

For the asymptotic stability analysis of EV aggregation delays, a typical electrical grid-electric vehicle system in [19] is adopted listing parameter values in Table I. Referring to [27], the power grid of the frequency regulation system is represented by three parts: speed governor, turbine, rotating mass and load. The speed governor controls the admission of steam to the turbine, which is represented by the speed droop $R$ and $\frac{1}{sT_g+1}$. The droop coefficient reflects the steady-state speed versus load characteristic of the generating unit, which equals to the ratio between frequency deviation and change in valve gate position. $T_g$ is the time constant of governor reflecting the steady-state feedback loop from the shaft to the valve adjustment. The stored energy of high pressure and high-temperature steam is converted into the rotating energy by a steam turbine. Through a reheat, the steam leaving the high-pressure section is returned to the boiler for the efficiency improvement. Simplifying the time constant of crossover piping and low-pressure inlet volumes to 0, the relationship between the turbine torque and the valve position is modeled as $\frac{sF_pT_r+1}{(sT_c+1)(sT_r+1)}$. $T_r$ is the time constant of reheater, $F_p$ is the fraction of total turbine power generated by high-pressure part, the time constant $T_c$ is introduced considering main inlet volumes and steam chest. The part of rotating mass and load mimics all the generator and the motor loads in the power system with $\frac{1}{Ms+D}$. The rotating masses from grid generators provide the inertia $M$ to overcome the instant power imbalance. Because of motor loads in the power system, their electrical power changes with frequency due to the changes in motor speed, which introduces the damping coefficient $D$ in the power system.

The analyses are implemented in Matlab 2018b with m-script and verified through Simulink. A 0.1p.u. load change is imposed at 10s as the external disruption. The processor is Intel (R) Core (TM) i7-7500U CPU and the installed memory is 24.0 GB.

According to Table I and (14)-(15), the grid coefficient $\boldsymbol{A}_{EG}$ and EV coefficient $\boldsymbol{A}_{EV}$ are obtained

$$\boldsymbol{A}_{EG}=\begin{bmatrix} -0.11 & 0.11 & 0 & 0 & 0 \\ 0 & -0.08 & -0.47 & 0.56 & 0 \\ 0 & 0 & -3.33 & 3.33 & 0 \\ -71.80 & 0 & 0 & -5 & -0.80 \\ 21 & 0 & 0 & 0 & 0 \end{bmatrix}, \boldsymbol{A}_{EV}=\begin{bmatrix} -1 & 0 \\ 0 & -1 \end{bmatrix} \quad (32)$$

The eigenvalues of the corresponding damping ratio of $\boldsymbol{A}_{EG}$ and $\boldsymbol{A}_{EV}$ are listed in Table II (a)-(b). The maximum damping ratio of $\boldsymbol{A}_{EG}$ is 1, while the value is 0.25. Besides, both eigenvalues of $\boldsymbol{A}_{EV}$ are -10. It reflects that the electrical grid and aggregated EV system can provide sufficient damping to maintain respective asymptotic stability. To detect the asymptotic stability of whole system without time delays, the eigenvalues of $(\boldsymbol{A}+\boldsymbol{A}_1+\boldsymbol{A}_2)$ in (16) are further calculated assuming $\tau_{EV}^1=\tau_{EV}^2=0$. Seen from the blue part of Table II, the involvement of EV system further enhances the electrical grid stability, which increases the damping ratio from 0.25 to 0.33.

TABLE II EIGENVALUES AND DAMPING RATIOS WITHOUT DELAYS

| | Eigenvalues | Damping ratios |
|---|---|---|
| (a) Electrical grid | -5.3724 | 1 |
| | -2.7440 | 1 |
| | -0.1034+ *j*0.4038 | 0.25 |
| | -0.1034- *j*0.4038 | 0.25 |
| | -0.2070 | 1 |
| (b) Aggregated EVs | -10 | 1 |
| | -10 | 1 |
| (c) Electrical grid-EV | -5.3823 | 1 |
| | -2.7264 | 1 |
| | -0.1738+ *j*0.4997 | 0.3285 |
| | -0.1738- *j*0.4997 | 0.3285 |
| | -0.1628 | 1 |
| | -9.9112 | 1 |
| | -10 | 1 |

### B. *Single Aggregation Delay*

Assuming the two EV aggregation delays are identical $\tau_{EV}^1=\tau_{EV}^2=\tau$, the zero-delay coefficient $(\boldsymbol{A}+\boldsymbol{A}_1+\boldsymbol{A}_2)$ is disassembled to the non-delay component $\boldsymbol{A}$, and single-delay component

$$\boldsymbol{A}\big|_{\tau_{EV}^1=\tau_{EV}^2}=\boldsymbol{A}_1+\boldsymbol{A}_2=\begin{bmatrix} 0 & 0 & 0 & 0 & 0 & 0 & 0 \\ 0 & 0 & 0 & 0 & 0 & 0 & 0 \\ 0 & 0 & 0 & 0 & 0 & 0 & 0 \\ 0 & 0 & 0 & 0 & 0 & 0 & 0 \\ 0 & 0 & 0 & 0 & 0 & 0 & 0 \\ -4.20 & 0 & 0 & 0 & -0.20 & 0 & 0 \\ -4.20 & 0 & 0 & 0 & -0.20 & 0 & 0 \end{bmatrix} \quad (33)$$

The time-delay coefficient in (33) is sparse with only four elements are non-zero. The eigenvalues of $\boldsymbol{A}$ are -10, -10, -5.37, -2.74, -0.21, -0.10± *j*0.40, while all eigenvalues of $\boldsymbol{A}\big|_{\tau_{EV}^1=\tau_{EV}^2}$ are 0. Due to the inaccessibility of $(\boldsymbol{A}+\boldsymbol{A}_1e^{-\lambda_1\tau_{EV}^1}+\boldsymbol{A}_2e^{-\lambda_2\tau_{EV}^2})$ eigenvalues, the delay distorted matrix $\boldsymbol{A}_N$ in (28) is formed with $N$=10 as an example. If the eigenvalues are in the left half-plane of the complex domain, the hybrid system is asymptotically stable, otherwise instability would be triggered. According to the eigenvalues calculated, the stability area of

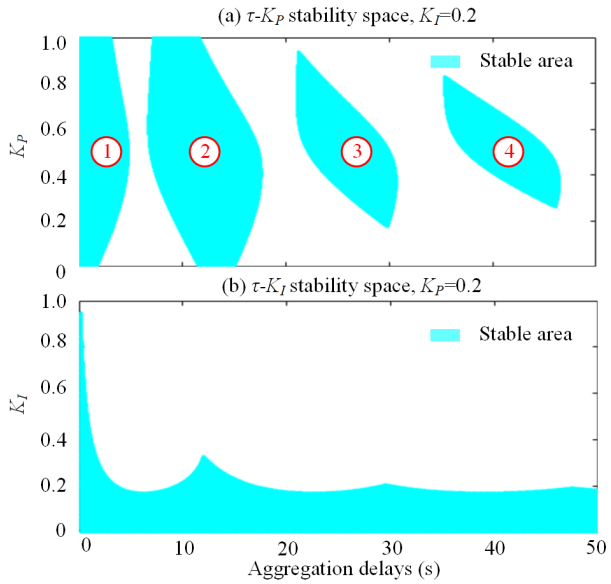


Fig. 8. Distorted stability space in $\tau$-$K_P$ and $\tau$-$K_I$ domains.

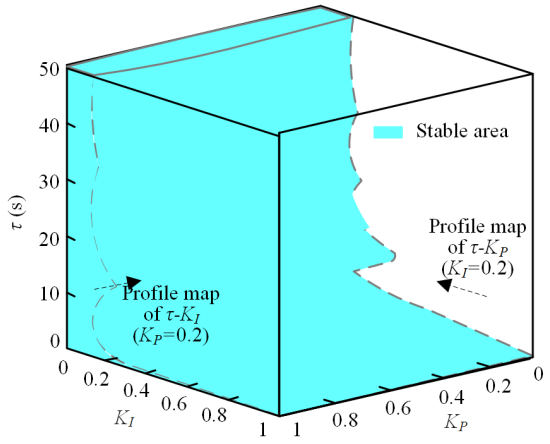


Fig. 9. Stable area in the $K_P$-$K_I$-$\tau$ space.

the electrical grid-electric vehicle system is depicted in Fig. 8, where $\tau$-$K_P$ and $\tau$-$K_I$ spaces are both distorted by the two aggregation delays. These two domains are extracted from the $K_P$-$K_I$-$\tau$ space in Fig. 9 to reflect the different delay impacts interacting with $K_P$ and $K_I$. To help the explanation of $K_P$-$K_I$-$\tau$ space, these two profile maps at $K_I$=0.2 and are $K_P$=0.2 are respectively formulated $K_P$-τ- and $K_I$-τ directions. After that, the profile maps are rotated to unify the horizontal axis as the aggregation delay, which generate the figures of those two domains in Fig. 8. The distorted approaches are different for the

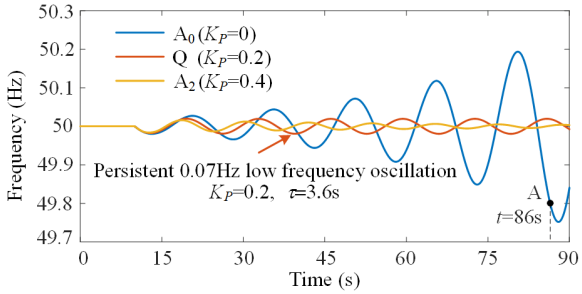


Fig. 10. Persistent low frequency oscillation with $K_P$=0.2, $\tau_{max}$=3.6s.

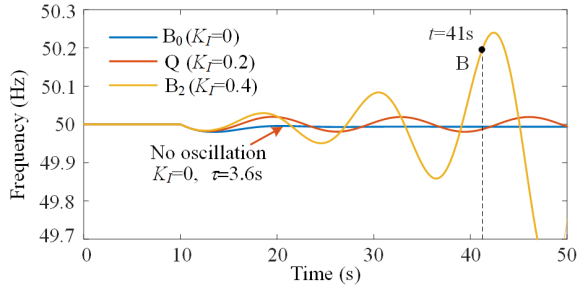


Fig. 11. Grid frequency fluctuations with $K_I$ from 0 to 0.4, $\tau_{max}$=3.6s.

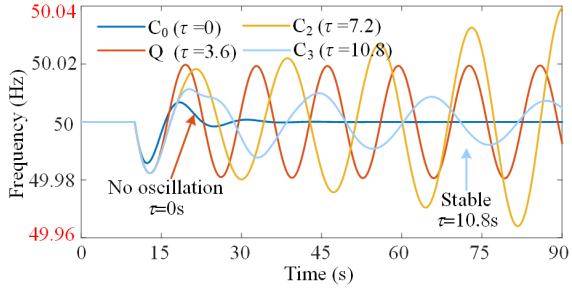


Fig. 12. Frequency waveforms with $\tau_{max}$ from 3.6s to 10.8s, $K_P$=0.2, $K_I$=0.2.

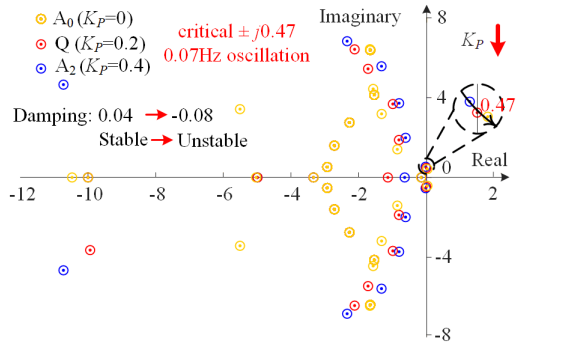


(a) Mode I: Eigenvalues crossing with $K_P$ from 0.4 to 0, τ=3.6s.

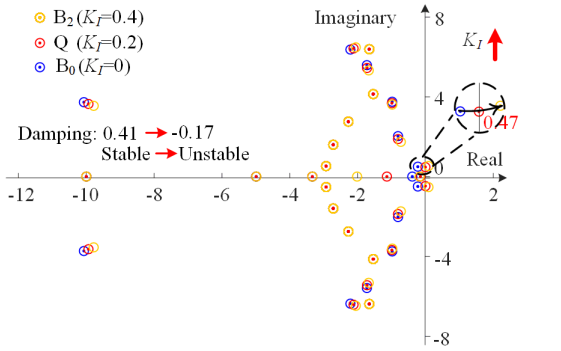


(b) Mode II: Eigenvalues crossing with $K_I$ from 0 to 0.4, τ=3.6s.

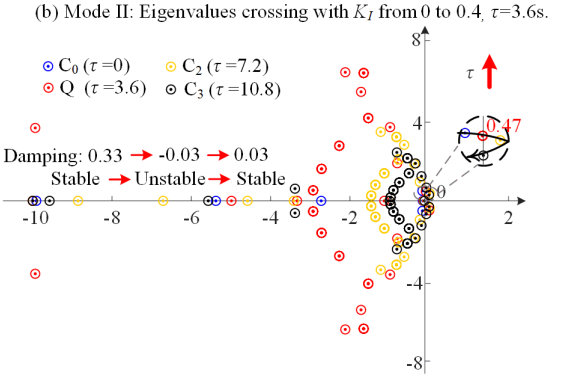


(c) Mode III: Eigenvalues crossing with $\tau_{max}$ from 3.6s to 10.8s, $K_P$=0.2, $K_I$=0.2.

Fig. 13. Three unstable modes.

proportional and integral controllers. In Fig. 8(a), the $\tau$-$K_P$ space is divided into four isolated stable areas, while a small continuous stable area is left in the $\tau$-$K_I$ space. To explore the instability mechanism, the frequency waveforms at $A_0$($\tau_{max}$=3.6s, $K_P$=0), Q($\tau_{max}$=3.6s, $K_P$=0.2), $A_2$($\tau_{max}$=3.6s, $K_P$=0.4) are shown in Fig. 10.

Coinciding with the distorted stability space in Fig. 8, *f* persistently oscillates at Q in Fig. 10, i.e., $K_P$=0.2, $\tau_{max}$=3.6s. Through the detection of the oscillation amplitude in the simulation waveform, the accuracy level of the proposed method can reach 0.0001s. Taken this critical point Q as an example, the exact value calculated by the developed method is 3.5866s. The oscillation amplitude of frequency waveform decreases at $\tau$=3.5866s, while the amplitude increases at $\tau$=3.5867s, which indicates the method accuracy can reach 0.0001s. The frequency deviation is within ±0.02Hz, and the oscillation frequency is 0.07Hz. When $K_P$=0.4, the disturbance caused by the external load gradually attenuates due to the adequate system damping. However, the frequency stability cannot be maintained at $A_0$, i.e., $K_P$=0, $\tau_{max}$=3.6s, which breaks the frequency variation range at *t*=86s, i.e., Point A.

TABLE III EIGENVALUE VARIATIONS WITH THE AGGREGATION DELAY

| $\tau$=0s | $\tau$=3.6s | $\tau$=7.2s | $\tau$=10.8s |
|---|---|---|---|
| –10 | –10 | –10 | –10 |
| –9.91 | –9.94 ± *j*3.64 | –8.86 | –9.58 |
| –5.38 | –4.99 | –4.58 | –5.57 |
| –2.72 | –2.12 ± *j*6.42 | –1.22 ± *j*3.44 | –0.82 ± *j*2.42 |
| –0.16 | –0.12 | –0.13 | –0.15 |
| –0.17± *j*0.50 | ± *j*0.47 | 0.01± *j*0.36 | 0.01± *j*0.29 |

To compare with the $K_P$ influence in Fig. 10, the integral gain is varied in Fig. 11 corresponding to B$_0$($\tau_{max}$=3.6s, $K_I$=0), Q($\tau_{max}$=3.6s, $K_I$=0.2), B$_1$($\tau_{max}$=3.6s, $K_I$=0.4). Having the same aggregation delay, it can be seen that the frequency stability rapidly loses at Point B after only 41s, which means the coupling of $K_I$ and $\tau$ is tighter than $K_P$. Moreover, the blue line with $K_I$=0 shows no oscillation, which shows enough damping facing the 3.6s aggregation delays. Comparing the orange curve ($K_P$=0, $K_I$=0.2, $\tau_{max}$=3.6s) in Fig. 10 and the blue curve ($K_P$=0.2, $K_I$=0, $\tau_{max}$=3.6s) in Fig. 11, it indicates that the non-zero values of $K_I$ and $\tau$ contribute more to the time-delay instability.

For further verification of this phenomenon, the aggregation delay is changed from 0 to 10.8s in Fig. 12. Coinciding with the distorted stability space, the grid frequency is asymptotically stable under both 0s and 10.8s aggregation delays, but instability occurs with $\tau_{max}$=7.2s. The stability space of $\tau$-$K_P$ is distorted due to the EV aggregation delays. The damped waveform with $\tau$=0s also verifies that the coupling of $K_I$ and $\tau$ is the main factor triggering the frequency instability because of the accumulated error in the integral controller.

The eigenvalue traces of Fig. 10 to 12 are depicted in Fig. 13(a)-(c), respectively. It can be seen that three unstable modes are targeted with the same pair of conjugate eigenvalues from electrical grid, which crosses the imaginary axis at ±*j*0.47. In Fig. 13(a), the instability happens when $K_P$ decreases below 0.2, while the increasing values of $K_I$ and $\tau$ lead to the system oscillation in Fig. 13(b)-(c). According to (29), the damping ratio variations of these three modes are also shown in Fig. 13, where the critical $\xi$ experiences the largest change in Mode II from 0.41 to -0.17. As the delay rises, a periodical stable phenomenon occurs, which is caused by the back and forth of the conjugate eigenvalues in Fig. 13(c). The eigenvalues in Fig. 13(c) is further listed to clearly explain the modes affected by the delay. Since the delayed system induces an infinite number of complex eigenvalues, the variation of the seven eigenvalues at $\tau$=0s is displayed as examples. Except for -10, other modes of the system are affected by the delay in Table III. Not only the value is varied, the eigenvalue number is also changed due to the delay. For example, the second eigenvalue –9.91 is replaced by the conjugate eigenvalues –9.94+ *j*3.64 and –9.94– *j*3.64 when $\tau$=3.6s. As the delay increases, this conjugate eigenvalue pair is reduced to a real value when $\tau$=7.2s and $\tau$=10.8s. The value and the number are both changed due to the aggregation delays. In Table IV, the magnitudes of $\tau$ and $K_I$ sensitivities are both around 2 times larger than that of $K_P$, which indicates the coupling of $\tau$ and $K_I$ triggers the frequency instability through the most fragile eigenvalue in the electrical grid.

TABLE IV CRITICAL EIGENVALUES SENSITIVITIES

| Critical eigenvalues | $\tau$ | $K_P$ | $K_I$ |
|---|---|---|---|
| + *j*0.47 | 0.12– *j*0.28 | –0.05+ *j*0.13 | 0.25+ *j*0.13 |
| – *j*0.47 | 0.12+ *j*0.28 | –0.05– *j*0.13 | 0.25– *j*0.13 |
| Sensitivity magnitude | 0.30 | 0.14 | 0.28 |

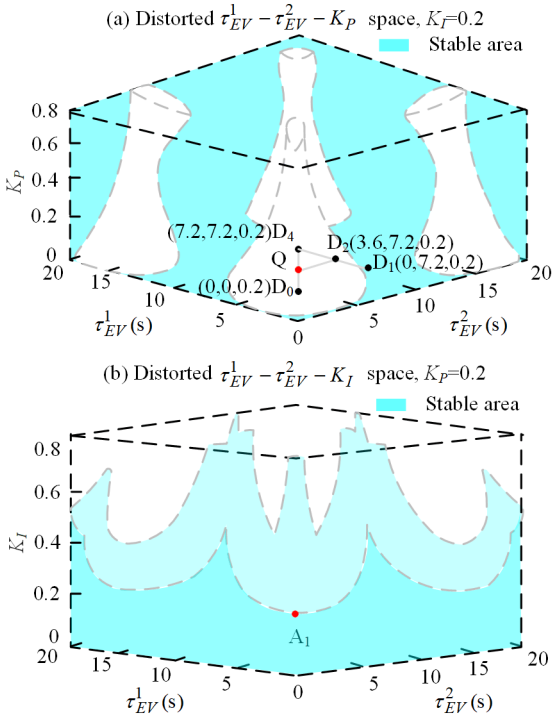


Fig. 14. Distorted stability spaces in heterogeneous-delay domains.

### C. Heterogeneous Aggregation Delays

During practical dispatch, the aggregation delays of different EV aggregators are often different, which introduces heterogeneous delays in the whole system. To investigate the heterogeneous-delay impact, the stable areas in $\tau_{EV}^1-\tau_{EV}^2-K_P$ and $\tau_{EV}^1-\tau_{EV}^2-K_I$ spaces are described in Fig. 14.

From Fig. 14, it can be seen that the whole stability region is dependent on a nonlinear interaction between the delays of the two aggregators. Furthermore, the dominant eigenvalue routes, which first leads to the instability, are plotted in Fig. 15 to explore the instability mechanism. Marked by the red line, it is found that $\tau_{EV}^1$ and $\tau_{EV}^2$ both affect the same target eigenvalues. The instability occurs only if both delays exceed 3.6s. Otherwise, the instability is not triggered.

The accuracy difference between proposed method and the stability criteria in [19], [28] is shown in Fig. 16. It can be seen from Fig. 16(a) that the proposed method is able to precisely determine the stability space of two aggregation delays. In the [0, 25s] × [0, 25s] stability space, it is revealed by the developed method that the aggregation delays induce four

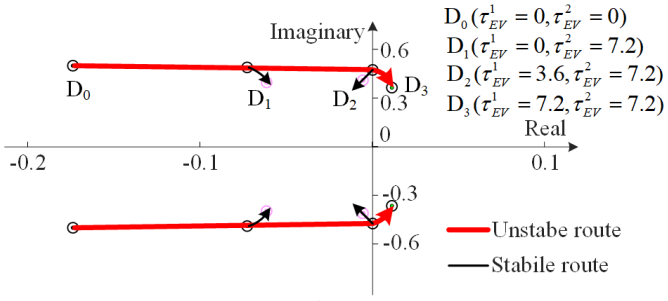


Fig. 15. Instability triggering route of heterogeneous aggregation delays.

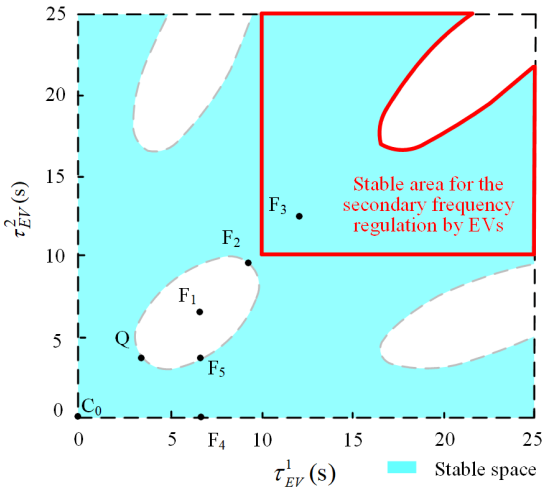


(a) Accurate stability space by the proposed method

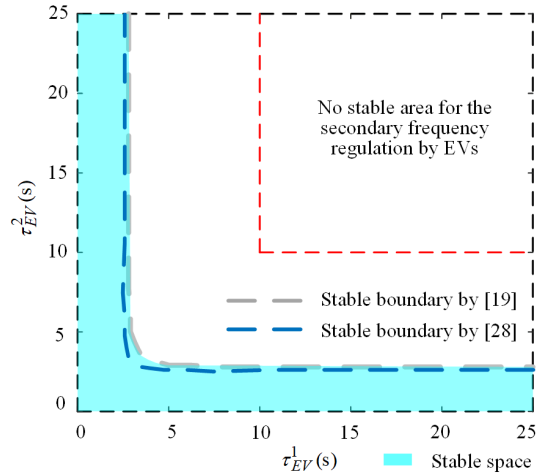


(b) Stability space by the methods in [19] and [28]

Fig. 16. Distorted stability space of two aggregation delays.

unstable holes, while the existing methods in Fig. 16 (b) cannot reveal this phenomenon and obtain small stability regions. Table V lists the computation time of the two-delay scenario for the efficiency comparison. Seen from Table V, the proposed method averagely takes only 0.072s for the assessment of each point in the stability space. However, the time domain stability criteria in [19] and [28] take 1008.260s and 1815.543s, respectively. Since 37 matrices are required to be solved by the existing method in [19] and 32 matrices to be calculated in [28], the assessment time of existing approaches is longer than the delay distorted matrix derived by the proposed method.

According to the regional transmission organization PJM [12], the timeframe of secondary frequency regulation is 1-10 minutes. When the number of EV supply equipment is more than 350, it was reported in [29] that the average delay from dispatch message arrival at EV aggregator to the scheduling

TABLE V ASSESSMENT EFFICIENCY COMPARISONS

| | Proposed method | Existing method [19] | Jensen inequality-based criterion [28] |
|---|---|---|---|
| Average assessment time for each point in the stability space | 0.072s | 1008.260s | 1815.543 |

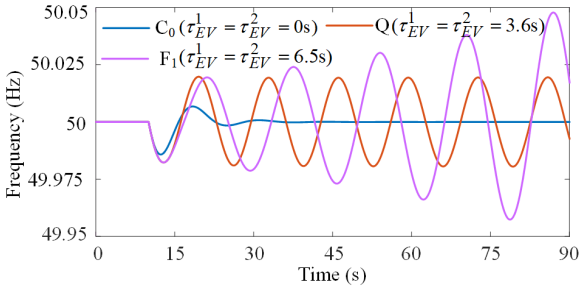


Fig. 17. The frequency instability due to delay increase.

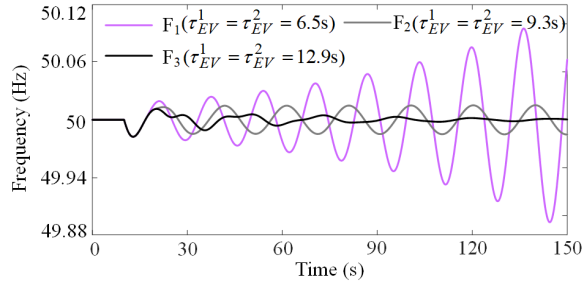


Fig. 18. The frequency re-stabilization because of unstable hole induced by the delays.

message arrival at EVs would be larger than 10s. Therefore, the aggregation delay could be in the range of 10s to 10mins. If the existing technique is employed, it is seen from Fig. 16 (b) that the EV aggregators will not provide the ancillary service because there is no stable area. However, referring to the stable delay area obtained by the proposed method, the EV aggregators are still able to participate in the frequency regulation to secure the grid stability within the red curve in Fig. 16(a).

According to the distorted stability space determined in Fig. 16(a), the grid frequency waveforms at $C_0$( $\tau_{EV}^1 = \tau_{EV}^2 = 0$s ), Q( $\tau_{EV}^1 = \tau_{EV}^2 = 3.6$s ), $F_1$( $\tau_{EV}^1 = \tau_{EV}^2 = 6.5$s ), $F_2$ ( $\tau_{EV}^1 = \tau_{EV}^2 = 9.3$s ), $F_3$( $\tau_{EV}^1 = \tau_{EV}^2 = 12.9$s ), $F_4$ ( $\tau_{EV}^1 = 6.5\text{s}, \tau_{EV}^2 = 0$s ), $F_5$( $\tau_{EV}^1 = 6.5\text{s}, \tau_{EV}^2 = 3.6$s ) are simulated to indicate the three delay effects of frequency instability due to delay increase, unstable hole, and heterogeneous-delay interaction.

➢ **The frequency instability due to delay increase ($C_0$, Q, $F_1$)**

The consequence of growing delay value is shown in Fig. 17. With the aggregation delays $\tau_{EV}^1$ and $\tau_{EV}^2$ raised from 0s to 6.5s, the system damping is gradually reduced leading to the frequency instability. In the delay scenario of $F_1$ ( $\tau_{EV}^1 = \tau_{EV}^2 = 6.5$s ), the frequency deviation grows to 50.05Hz facing a 0.1 p.u. disturbance. This phenomenon can be explained by the aggregation delay model (16) of hybrid system. The divergent oscillation is caused by the coupling of time and delays in $\sum_{i=1}^{n} \boldsymbol{A}_i \boldsymbol{x}(t-\tau_{EV}^i)$. As $\boldsymbol{A}_i$ ($i$=1,…,$n$) are made up of the charging and discharging coefficients $K_{EV}^i$, battery time constant $T_{EV}^i$, and automatic generation control (AGC) parameters, the power aggregation state of EVs can be reflected

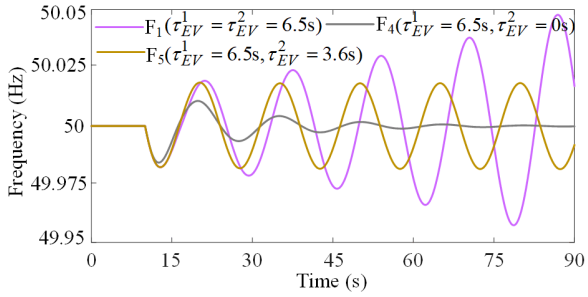


Fig. 19. The heterogeneous-delay interaction.

by $\sum_{i=1}^{n} \boldsymbol{A}_i \boldsymbol{x}(t-\tau_{EV}^i)$. The larger $\tau_{EV}^1$ and $\tau_{EV}^2$ would disorder the normal participation of EVs more seriously via the $t-\tau_{EV}^i$, which enlarges the grid frequency oscillation.

➢ **The unstable hole induced by the delays ($F_1$, $F_2$, $F_3$)**

The simulations at $F_1$, $F_2$, $F_3$ are presented in Fig. 18 to depict the unstable hole induced by the delays. When the aggregation delays continue growing to 12.9s in Fig. 18, the oscillation of frequency waveform is gradually reduced in the black curve. The characteristic equation of the aggregation delay model (16) can be expressed as

$$\det\left(s\boldsymbol{I}-\boldsymbol{A}-\sum_{i=1}^{n}\boldsymbol{A}_i e^{-\tau_{EV}^i s}\right)=0 \tag{34}$$

Due to the transcendental items $e^{-\tau_{EV}^i s}$, $i$=1,…,$n$, introduced by aggregation delays, the periodic eigenvalue crossing of the imaginary might occur as the delay increase. This induces unstable holes in the stability space distorting the continuity of stable area.

➢ **The heterogeneous-delay interaction ($F_1$, $F_4$, $F_5$)**

To investigate the interaction of heterogeneous delays, the grid frequency performance facing heterogeneous delays is displayed in Fig. 19. By the decrease of $\tau_{EV}^2$ from 6.5s to 0s, it can be seen that the frequency fluctuation is secured within [-49.98Hz, 50.02sHz]. Despite the existence of aggregation delay $\tau_{EV}^1=6.5$s, the system stability is notably maintained by avoiding the identical aggregation delay value. If the aggregation delays are identical, the delayed power from various EV aggregators would directly couple with each other via $\sum_{i=1}^{n}\boldsymbol{A}_i$, which aggravates delay instability shown at $F_1$.

To further investigate the heterogeneous-delay impact, the scenario of three aggregation delays with one more EV aggregator is shown in Fig. 20. It can be seen that the interaction of three heterogeneous delays further leads to eight isolated unstable areas in the range of [0,25s] × [0,25s] × [0,25s], which breaks the continuity of delay stability space. From the stability space of two aggregation delays in Fig. 16(a) and that of three aggregation delays in Fig. 20, due to heterogeneous delays, not only the number of unstable areas increases with the participation of more EVs, the diverse shapes of those unstable areas also imposes more unstable risks for the whole grid-vehicle system.

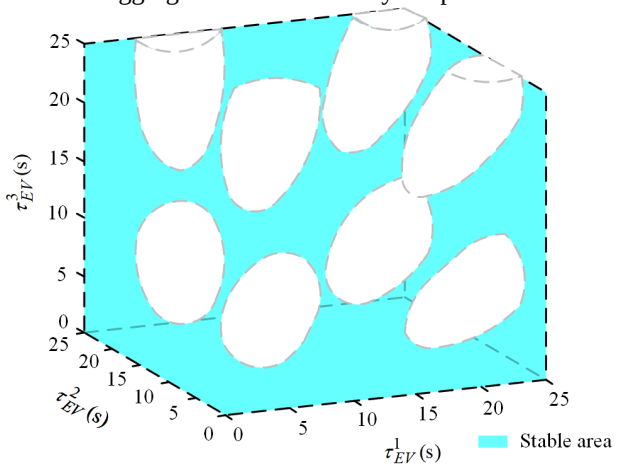


Fig. 20. Distorted stability space of three EV aggregators.

### *D. Mechanism Discussion and Control Design Guidance*

According to the determined stability space, the dissection of three sequential paths benefits the identification of three different roles in the relationship between EV aggregation delays and grid frequency: prerequisite, aggravation, distortion.

**Control path (prerequisite):** The $K_P$ and $K_I$ controllers represent the AGC components for instant deviation and accumulative deviation regulations, respectively. From Table IV, it can be seen that $K_I$ and $\tau$ almost contribute the same to the system instability around 0.30. The magnitudes of $\tau$ and $K_I$ sensitivities are both around 2 times larger than that of $K_P$, which indicates the $\tau$ and $K_I$ coupling is the prerequisite for the instability risk of aggregation delay.

**Combination path (aggravation):** From the stability space in Fig. 8, the combination of proportional control channel ($K_P$, $\tau$) and integral control channel ($K_I$, $\tau$) further aggravates the stability space. Different from the continuous stable area in $\tau$-$K_I$ space of Fig. 8(b), the participation of proportional control channel ($K_P$, $\tau$) chops the stable space into several isolated fragments in Fig. 8(a).

**Coupling path (distortion):** Besides the effects from the control and combination paths, the hybridization of various EV aggregators further distorts the stability space due to the heterogeneous-delays. It can be seen from Fig. 16(a) that, due to the two EV aggregation delays, the continuous stable areas are distorted by four unstable holes.

However, without the path dissection, these three sequential paths would be lumped as one process, which can only obtain a bound value for the aggregation delays. It is unable to find out their different roles related to the aggregation delay instability.

Targeted these three paths and their respective roles in triggering the instability, the step-by-step guidance can be made to controller design for the asymptotic stability

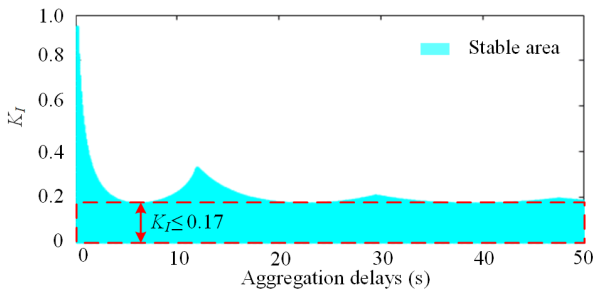


Fig. 21. Maximum limitation of $K_I$ for the stable area continuity.

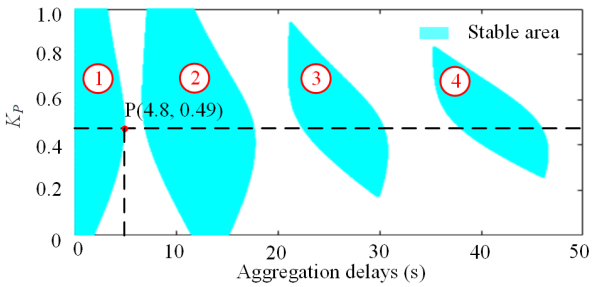


Fig. 22. Local extreme point $K_P$ for the isolation gap minimization.

improvement.

➢ **Control path (limit maximum $K_I$ to enlarge the stable area continuity):** As the coupling of $K_I$ and $\tau$ is the main reason inducing the instability risk. The maximum value of $K_I$ could be set to reduce this risk. In Fig. 21, there is a $K_I$ range of (0, 0.17], in which the allowable aggregation delay can continuously reach 50s. By limiting the maximum value of $K_I$ within 0.17, the continuity of stable area for the aggregation delay can be significantly guaranteed.

➢ **Combination path (select local extreme point for $K_P$ to minimize the isolation gap):** Considering the combination with the proportional control loop, the proportional gain $K_P$ is then increased to further enhance the asymptotic stability and the regulation dynamic. As can be seen from Fig. 22, there exists an extreme point P in the first continue stable area, which maximizes the aggregation delay range even if the stable area is chopped into four isolated fragments.

➢ **Coupling path (avoid the resonance of heterogeneous aggregation delays):** As can be seen from Fig. 23, the minimum delay value is reached at Q(3.6s,3.6s), where the two aggregation delays are identically coupled. If the two aggregation delays $\tau_{EV}^1$ and $\tau_{EV}^2$ are different, the tolerant aggregation delay point is extended to $Q_1$(3.6s,17.1s). The allowable aggregation time for the second EV aggregator is able to increase from 3.6s to 17.1s. Thus, the avoidance of various delay resonance helps to improve the asymptotic stability of the system.

In the practical method, the control gains are usually determined through three procedures: model derivation, stability analysis, control performance simulation.

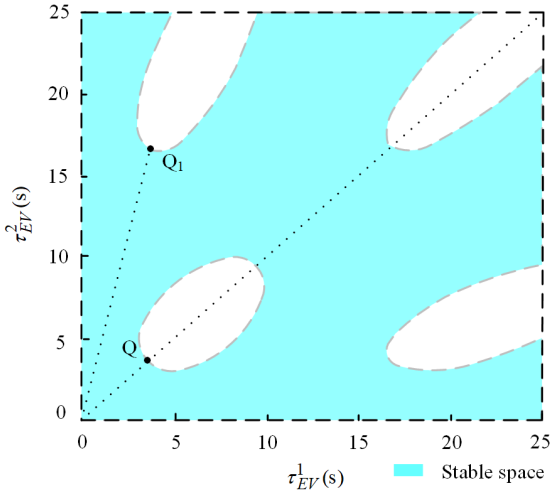


Fig. 23. Avoiding heterogeneous aggregation delay resonance.

In the procedure of model derivation, the main concern and the key components should be effectively represented in the system model. As the main concern of this work is the aggregation delays and the key component is the electrical grid-electric vehicle system, the concise integration of these factors is necessary for the following analysis.

With the derived model, the accurate and efficient stability assessment plays an important role in the tuning of the control gains. If the result is conservative, the controller performance cannot be optimized. Besides, the speed of analysis method should also be guaranteed.

On the basis of the model and stability assessment results, the range of control gain is effectively and efficiently determined. Depending on the accuracy of gain range provided by the analysis, the simulation is implemented to test the control gains to guarantee the controller performance.

The established model, analysis method, and simulation efficiency contribute to the complexity of the control gain tuning. It can be seen that the accurate, efficient and systematic stability approach dominates the controller performance and the tuning efficiency, especially considering huge amount of electric vehicles with various gains.

## V. Conclusions

To address the aggregation delay uncertainties caused by electric vehicles during the grid frequency regulation, the precise stability space is determined by the proposed analysis method, which discovers the distorted stability space and triggering mechanism of system instability. Heterogeneous time delays during EV aggregations infect the system through control, combination, and coupling procedures disturbing the power dispatch with asynchronous frequency signals and reconfiguring a delay distorted matrix for the electrical grid-electric vehicle system.

Due to the deviation accumulation, the influence of EV aggregation delays mainly penetrates through the integral controller. By the form of low-frequency oscillation, the most fragile eigenvalue in the electrical grid is targeted by heterogeneous delays, which is manipulated to distort the stability space of grid frequency. Moreover, the distortion of stability space reveals three unstable modes of the electrical grid-electric vehicle system. Due to the interaction among different aggregation delays, holes and folds are generated in the stability space. Because of the distorted stability space, heterogeneous delays between transmission system operators and aggregators providing frequency response need to be carefully considered to avoid the risky stability areas. The implications of the stability space and instability mechanism are standard PI tuning techniques designed for systems without delay may not be suitable for electrical vehicle aggregation.

## References

[1] National Electricity Transmission System Security and Quality of Supply Standard. [Online]. Available: https://www.nationalgrid.com/sites/default/files/documents/NETS%20SQSS%20V2.3.pdf
[2] PJM Manual 36. [Online]. Available: https://www.pjm.com/~/media/documents/manuals/m36.ashx.
[3] Power supply business rules. [Online]. Available: http://zjb.nea.gov.cn/article/zcfg/bmgz/201808/2911.htm.
[4] GridWatch frequency. [Online]. Available: https://gridwatch.co.uk/frequency.

[5] UK power cut: National Grid promises to learn lessons from blackout. [Online]. Available: https://www.bbc.co.uk/news/uk-49302996.
[6] J. B Goodenough. "Evolution of strategies for modern rechargeable batteries," *Acc. Chem. Res.*, vol. 46, no. 5, pp. 1053-1061, 2012.
[7] J. B. Goodenough, and Y. Kim. "Challenges for rechargeable Li batteries". *Chem. Mater.*, vol. 22, no. 3, pp. 587-603, 2009.
[8] Tesla Q4 2018 Vehicle Production & Deliveries, Also Announcing $2,000 Price Reduction in US. [Online]. Available: https://ir.tesla.com/news-releases/news-release-de tails /tesla-q4-2018-vehicle-production-deliveries-also-announcing-2000.
[9] Tesla, Inc. [Online]. Available: https://en.wikipedia.org/wiki/Tesla,_Inc.
[10] State Council of Republic of China State: "The national medium- and long-term program for science and technology development (2006-2020)". [Online] Available: https://www.itu.int/en/ITU-D/Cybersecurity/Documents/National_Strategies_Repository/China_2006.pdf.
[11] Qin Pro EV. [Online]. Available: http://www.bydauto.com.cn/auto/news/2019-05-16/1502368 195703.
[12] Primary Frequency Response Stakeholder Education. [Online]. Available: https://www.pjm.com/~/media/committees-groups/task-forces/pfrstf/20170901/20170901-primary-frequency-response-education-part-1-of-2.ashx.
[13] K. Kaur, N. Kumar, and M. Singh. "Coordinated power control of electric vehicles for grid frequency support: MILP-based hierarchical control design," *IEEE Trans. Smart Grid*, vol. 10, no. 3, pp. 3364-3373, 2018.
[14] B. Vatandoust, A. Ahmadian, M.A. Golkar, A. Elkamel, A. Almansoori, and M. Ghaljehei. "Risk-averse optimal bidding of electric vehicles and energy storage aggregator in day-ahead frequency regulation market," *IEEE Trans. Power Syst.*, vol. 34, no. 3, pp. 2036-2047, 2019.
[15] C. Mu, W. Liu, and W. Xu. "Hierarchically adaptive frequency control for an EV-integrated smart grid with renewable energy," *IEEE Trans. IEEE Trans. Ind. Informat.*, vol. 14, no. 9, pp. 4254-4263, 2018.
[16] Y. Mu, J. Wu, N. Jenkins, H. Jia, and C. Wang. "A spatial-temporal model for grid impact analysis of plug-in electric vehicles," *Applied Energy*, vol. 114, pp: 456-465, 2014.
[17] M. Wang, Y. Mu, F. Li, H. Jia, X. Li, Q. Shi, and T. Jiang. "State space model of aggregated electric vehicles for frequency regulation," *IEEE Trans. Smart Grid*, in press, 2019.
[18] M. Arani, and, Y. Mohamed. "Cooperative control of wind power generator and electric vehicles for microgrid primary frequency regulation," *IEEE Trans. on Smart Grid*, vol. 9, no. 6, pp.5677-5686, 2018.
[19] K. Ko, and D. K. Sung. "The effect of EV aggregators with time-varying delays on the stability of a load frequency control system," *IEEE Trans. Power Syst.*, vol. 33, no. 1, pp. 669-680, 2018.
[20] H. Fan, L. Jiang, C. Zhang, and C. Mao. "Frequency regulation of multi-area power systems with plug-in electric vehicles considering communication delays," *IET Gener. Transm. Distrib.*, vol. 10, no. 14, pp. 3481-3491, 2016.
[21] H. Jia, X. Li, Y. Mu, C. Xu, Y. Jiang, X. Yu, J. Wu, and C. Dong. "Coordinated control for EV aggregators and power plants in frequency regulation considering time-varying delays," *Applied Energy*, vol. 210, pp: 1363-1376, 2018.
[22] F. Milano. "Small-signal stability analysis of large power systems with inclusion of multiple delays." *IEEE Trans. Power Syst.*, vol.31, no. 4, pp. 3257-3266, 2016.
[23] J. V Lambers and A. C. Sumner. *Explorations in numerical analysis*. World Scientific, pp. 216, 2018.
[24] J. K. Hale, L. Verduyn, M. Sjoerd. *Introduction to functional differential equations*. Applied Mathematical Science, 1993.
[25] J. C. Mason, and D. C. Handscomb. *Chebyshev polynomials*. Chapman and Hall/CRC, 2002.
[26] E. Jarlebring, K. Meerbergen, and W. Michiels, "A Krylov method for the delay eigenvalue problem," SIAM J. Sci. Comput., vol. 32, no. 6, pp. 3278–3300, 2010.
[27] P. Kundur. *Power system stability and control*. New York: McGraw-Hill, 1994.
[28] C. Zhang, Y. He, L. Jiang, M. Wu. "Notes on stability of time-delay systems: bounding inequalities and augmented Lyapunov-Krasovskii functionals," *IEEE Trans Automat. Control*, vol. 62, no. 10, pp: 5331–5336, 2017.
[29] K. Ko, and D. K. Sung. "The effect of cellular network-based communication delays in an EV aggregator's domain on frequency regulation service," *IEEE Trans. Smart Grid*, vol. 10, no. 1, pp. 65-73, 2019.

**Chaoyu Dong** received the B.Sc. degree in electrical engineering from Tianjin University, China, in 2013.
His research interests include energy-information system stability and management.

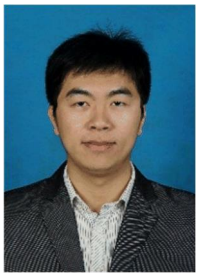

**Qian Xiao** (S'17-M'20) received the B.S. and M.S. degrees in electrical engineering from Hebei University of Technology, Tianjin, China, in 2011 and 2014 respectively, and Ph.D. degree in electrical engineering from Tianjin University, Tianjin, China, in 2020. From Oct. 2018 to Nov. 2019, he was a visiting scholar with the Department of Energy Technology, Aalborg University, Aalborg, Denmark.

From Jan. 2020, he is currently an Assistant Professor with the School of Electrical and Information Engineering, Tianjin University. His research interests are multilevel converters, DC/DC converters, and power electronics for distributed generation, microgrid, and HVDC.

**Mingshen Wang** (S'16) received the B.S. and M.S. degrees in electrical engineering from Tianjin University, Tianjin, China, in 2013 and 2016, respectively, where he is currently pursuing the Ph.D. degree in electrical engineering.

From 2017 to 2019, he was a Joint Ph.D. Student with the University of Tennessee, Knoxville, TN, USA. His research interests include modeling, operation, and control of demand side resources.

**Thomas Morstyn** (S'14-M'16) received the BEng (Hon.) degree from the University of Melbourne in 2011, and the PhD degree from the University of New South Wales in 2016, both in electrical engineering.

He is an EPSRC Research Fellow with the Department of Engineering Science at the University of Oxford, and he is a fellow with the Oxford Martin Programme on Integrating Renewable Energy. His research interests include multi-agent control and market design for integrating distributed energy resources into power system operations.

**Malcolm D. McCulloch** (SM'89) received the B.Sc. (Eng.) and Ph.D. degrees in electrical engineering from the University of the Witwatersrand, Johannesburg, South Africa, in 1986 and 1990, respectively.

In 1993, he joined the University of Oxford, Oxford, U.K., to head up the Energy and Power Group, where he is currently an Associate

Professor in the Department of Engineering Science. He is active in the areas of electrical machines, transport, and smart grids. His work addresses transforming existing power networks, designing new power networks for the developing world, developing new technology for electric vehicles, and developing approaches to integrated mobility.

**Hongjie Jia** (M'04-SM'17) received the B.S., M.S., and Ph.D. degrees in electrical engineering from Tianjin University, Tianjin, China, in 1996, 1999, and 2001, respectively.

He is currently a Professor with Tianjin University, Tianjin, China. His research interests include power reliability assessment, stability analysis and control, distribution network planning and automation, and integrated energy system.